Journal of Cultural Heritage 37 (2019) 29–43

Available online at
ScienceDirect
www.sciencedirect.com

Elsevier Masson France
EM|consulte
www.em-consulte.com/en

Original article

Daraki-Chattan rock art constrained OSL chronology and multianalytical techniques: A first pilot investigation

Ioannis Liritzis[a,b,*], Robert Bednarik[c,d], Giriraj Kumar[d,e], George Polymeris[f], Ioannis Iliopoulos[g], Vayia Xanthopoulou[g], Nikos Zacharias[h], Asimina Vafiadou[b], Maria Bratitsi[b]

[a] University of Henan, Key Research Institute of Yellow River Civilization and Sustainable Development & College of Environment and Planning, Henan, Kaifeng 475001, China
[b] University of the Aegean, Lab of Achaeometry, Department of Mediterranean Studies, 1 Demokratias Str, Rhodes 85132, Greece
[c] International Federation of Rock Art Organizations, P.O. Box 216, Caulfield South, Melbourne, Vic. 3162, Australia
[d] International Centre for Rock Art Dating, Hebei Normal University, Shijiazhuang, China
[e] Rock Art Society of India, Faculty of Arts, Dayalbagh Educational Institute, Dayalbagh, Agra 282 005, India
[f] Ankara University, Institute of Nuclear Sciences, Tandoğan Campus, 06100 Beşevler, Ankara, Turkey
[g] University of Patras, Department of Geology, Rio Patras 265 04, Greece
[h] University of the Peloponnese, Department of History, Archaeology, and Cultural Resources Management, 24100 Kalamata, Greece

ARTICLE INFO

Article history:
Received 2 May 2018
Accepted 28 September 2018
Available online 30 November 2018

Keywords:
Dating
Luminescence
Rock art
Radiation dosimetry
Exfoliation
Weathering

ABSTRACT

The cave of Daraki-Chattan (in Rewa river, India) bears important palaeolithic rock art (petroglyphs), while the environs is exceptionally rich in stone tools, mostly of the Acheulian. The field survey and excavations in the area found cupule panel fragments almost down to bedrock; Acheulian industry to Oldowan-like industry including several hammerstones. Early work demonstrated that at least some of the petroglyphs were of the earliest documented occupation of the region. Exfoliated pieces and boulders from the rock surface were found in the sediments, some bearing cupules and grooves. Here a detailed methodological procedure is enacted consisting of luminescence dating reinforced by mineralogical issues, where the latter secures credibility of the former. The optically stimulated luminescence (OSL), of the luminescence versus depth profiles, following blue LED and Single Aliquot Regeneration (SAR) technique of quartz, was applied following the surface luminescence dating versions to date this fallen rock. The two dose profiles from the sandstone studies provided an average date for the fallen boulder in the 13th millennium, providing a constrained *terminus post quem*. Surface patina and intrusion of (Fe, Mn) aluminosilicate weathering solution was examined in both luminescence profiles, properly dealt with issues of X-Ray Diffraction (XRD), Scanning Electron Microscopy–Energy Dispersive Spectroscopy (SEM–EDS), X-Ray Florescence-Energy Dispersive mode (XRF/ED), Cathodoluminescence, stereomicroscope, thin sections optical microscopy (OM) and microdosimetry. Analytical petrographic results aided interpretation of luminescence data obtained.

From the above rationale the two ages obtained from the two profiles can be considered close within errors, that coincide with the drastic change from last glaciation transition to the milder climate of the Holocene and the sudden end of colder Younger Dryas in ~13th Ka BP, having an impact on the weathering, erosion and exfoliation of rock surfaces caused by the significant temperature change and the resulted thermal differential expansion of rocks (onset of the Holocene).

1. Introduction

The ongoing research of 'prehistoric' rock art outstays as one of the most intractable problems in archaeology and early cultural heritage since 1980s, in particular the last few years. Absolute dating of carved rock art (petroglyphs) and their complex characterization and interpretation is developed fast and the subject merits of special attention throughout the World [1,2]. Thus, any

* Corresponding author at: University of Henan, Key Research Institute of Yellow River Civilization and Sustainable Development & College of Environment and Planning, Henan, China.
E-mail address: liritzis@rhodes.aegean.gr (I. Liritzis).

https://doi.org/10.1016/j.culher.2018.09.018
1296-2074/

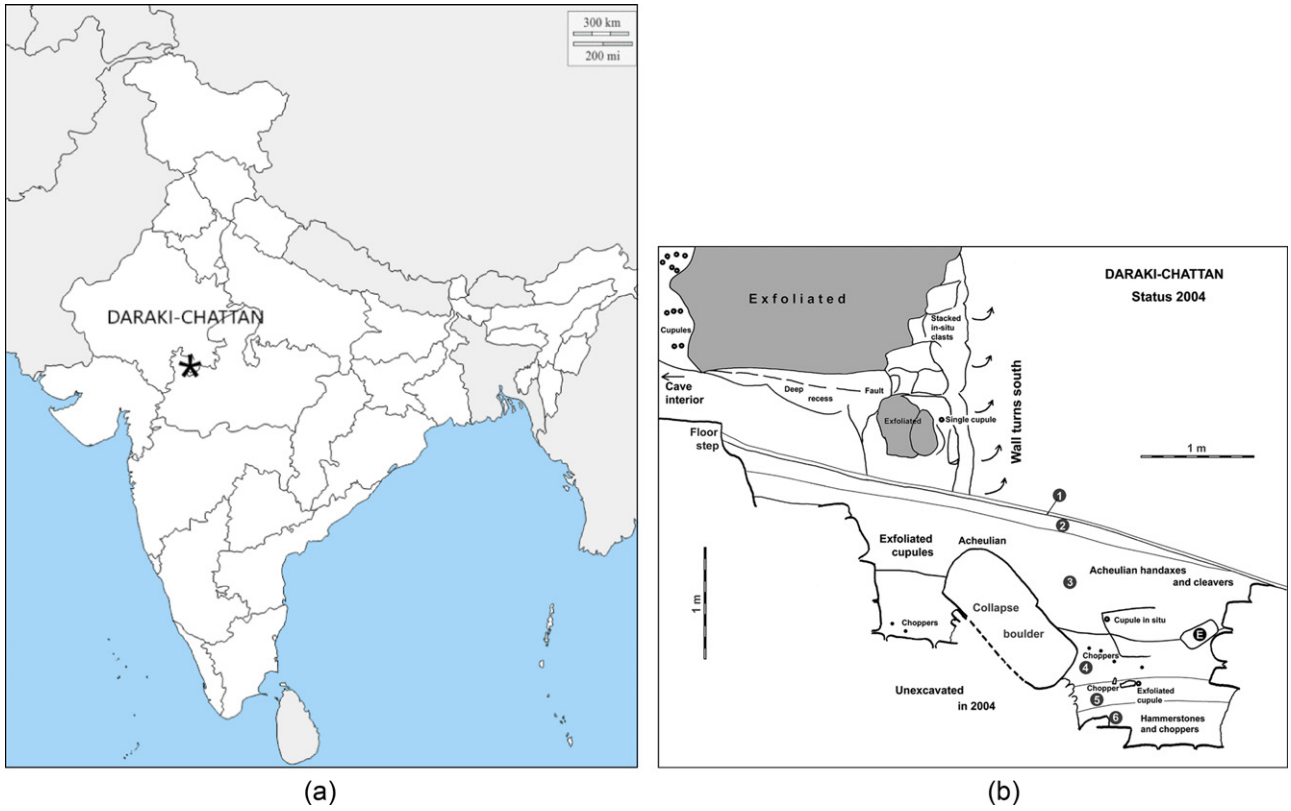

Fig. 1. (a) Map of India and the site. (b) The section of Daraki-Chattan rock art, stratigraphy and cave entrance. This map shows the location of sample DC-LIR-1 from boulder E. Numbers in black spots represent layers and other numbers the locations of measured environmental gamma radiation by the portable NaI scintillator [4,Fig. 26].

scientific study of rock art is crucially dependent upon some form of reliable dating of the art, its contextual archaeological evidence and the long history of any environmental impact. An ongoing work in Indian rock art is presented here. To the immediate north of the small town Bhanpura in Madhya Pradesh, central India, lies the Indragarh-Chanchala Mata plateau, surrounded by steep escarpments (Fig. 1).

Its western extension, Indragarh Hill, is overcovered by the ruins of an 8th century AD fort and it consists of Proterozoic quartzite. The cave of Daraki-Chattan is located in its western ramparts, overlooking the valley of the Rewa river. The area is exceptionally rich in stone tools, mostly of the Acheulian, which can be found in fluvial sediments of the Rewa, on the surface of plateaus and other deflation areas. They also occur on the surface of the floor of Daraki-Chattan Cave (N 24°32.100′, E 75°43.840′, 420 m a.s.l.). The narrow quartzite cave features 510 cupules on its two walls.

Discovered in 1993, subsequent investigations were started by Giriraj Kumar (1996, 2002–2008) and Bednarik. Most importantly, the cupules occurred not only in the Acheulian, but also in the Mode 1 deposit, and several hammerstones thought to have been used in the creation of cupules were also found in the lower parts of the lower strata. Therefore, this work demonstrated conclusively that at least some of the petroglyphs were of the earliest documented occupation of the cave (Fig. 1b). The upper half of the deposit contained a rich Acheulian industry, whereas the lower half an Oldowan-like Mode 1 industry [3].

Earlier optically stimulated luminescence (OSL) dating of three sediment samples from Daraki-Chattan and another four samples from Bhimbetka provided results that were inconclusive in that they included a major inversion at the latter site, and Holocene dates for Acheulian tools at the former site [3,4].

The surface luminescence dating (SLD) concerns rock surfaces where the resetting of the luminescence signal on surfaces was caused by exposure to solar radiation. Suitable rocks include sandstones, granites, marbles, limestones, schists and others that include quartz and feldspar minerals. The luminescence signal is measured by OSL where the sample in powder or slice form is exposed to LEDs or laser beam [5–10]. Initially sunlight luminescence analysis was used for dating sediment deposits that were well sun bleached prior to being covered by other layers that prevented the sun from reaching those sedimentary layers [13]. Later on the concept of dating rock surfaces in ancient monuments was initiated by Liritzis [12], then followed by Habermann et al. [13], and a review by Liritzis [14], Sohbati [15] and Scarre [16]. Here the rationale is the eviction of trapped electrons of geological luminescence and bleaching of luminescence of the upper millimetres of rock surface layers (its minerals of quartz and feldspars), once the block is overlain by another material, resetting the luminescence clock to zero. Thereafter luminescence within the rock increases from environmental radiation with time.

The solar radiation erases the electrons in the crystal lattice traps in the minerals of the rock (quartz, feldspar). Upon burial these traps are gradually refilled by environmental radiation derived from natural radioisotopes of the immediate vicinity of the rock sample. The bleached luminescence is a function of depth below surface, as well as the duration that the surface has been exposed to sun and sunlight intensity [5,17]. The remaining luminescence as a function of depth on a rock surface is a mathematical function that includes the age or the sun-exposure time from the moment of carving until today [18].

The application of the SLD method on rocks is an upcoming novel technique of absolute dating and has been reported earlier [5–15].

Thus, based upon the SLD principles for a continually exposed rock surfaces (i.e. not overlain by other rocks or sediment) a different version is followed for age calculation. After a rock surface has been carved, engraved or sculptured, be it for masonry or statues

or rock art [14], sun rays penetrate the fresh surface to a depth of at least 15 mm below surface, depending on the type of rock [5,17,18].

Here a pilot study of a quartzite exfoliated block bearing two engraved grooves, has been made through OSL measurements of two profiles (from the top where patina extends down to a depth of several millimetres), introducing a methodological approach. A thin section of the cut weathered quartzite profile was made and elemental analyses by SEM–EDS and XRF/EDS, mineralogical via optical microscopy (OM), XRD and cathodoluminescence were applied to evaluate the weathered state of diffused effect into the upper few centimetres' layers and investigate the obtained luminescence data of equivalent dose versus depth and providing first OSL age data. In fact the petrographic and mineralogical characterization of samples have a fundamental importance in luminescence dating and in the current work the relation between these data and the age results is documented.

2. Instrumentation for analysis

The analytical techniques applied to investigate the internal nature of the rock art piece included: (a) SEM–EDS (Laboratory of Electron Microscopy and Microanalysis, School of Natural Sciences, University of Patras, Greece – LEMM; Laboratory of Archaeometry, Department of History, Archaeology and Cultural Resources Management, University of the Peloponnese, Greece – LA); (b) cold cathodoluminescence microscopy (Laboratory of Mineral and Rock Research, Department of Geology, University of Patras, Greece – LMRR); (c) XRF–EDS (LEMM); (d) XRD (LMRR); (e) digital stereomicroscopy (Fitch Laboratory in the British School of Athens, Greece – FLBA); (f) thin section preparation and optical microscopy (LMRR).

Specifications of the setting and details of instrumentation used are the following: A JEOL 6300 Scanning Electron Microscope equipped with an EDX spectrometer (LEMM) was employed for the compositional analysis of the studied material on a carbon coated polished thin section under backscatter mode.

Various additional spot analyses were conducted on a JEOL (JSM-6510LV) SEM coupled with an EDX (Oxford Systems) spectrometer (LA). The analytical data were obtained by INCA software. The measurements were performed non-invasively and on intact surfaces using a removable, conductive carbon tape and at 20 kV accelerating voltage for 120 s count time.

The fresh surface cut remaining from preparing the thin section was analyzed by means of XRF/EDS using a NEX CG, Rigaku system (LEMM) with an X-ray tube with Pd anode which worked under a tube power of 50 W (50 kV to 2 mA). It is equipped with 5 secondary targets and a Silicon Drift Detector (SDD). Standardless analysis performed using RPF-SQX (Rigaku Profile Fitting – Spectra Quant X) software with a fundamental parameters method for accurate quantification combined with full profile fitting method.

The mineralogical and petrographic characteristics of the studied sample were obtained through the microscopic observation of the thin section under a Zeiss AxioScope.A1 polarizing microscope (LRMM) equipped with e Jena ProgRes C3 video camera.

An aliquot of the studied sample was ground to a <10 μm powder by using an agate mortar and was subsequently analyzed under a BRUKER D8 Advance X-Ray diffractometer, with Ni filtered Cu Kα radiation, operating at 40 kV/40 mA (LRMM). The interpretation of the acquired diffractograms and mineral identification was performed using DIFFRACplus EVA software (Bruker-AXS, Madison, WI, USA) based on the International Centre for Diffraction Data Powder Diffraction File (2006).

A Leitz Wetzlar Orthoplan Microscope on which a Reliotron III Cathodoluminescence system was attached was used (LRMM) for unveiling further compositional details of the mineral grains. The conditions used were 10 kV excitation voltage and 0.200–0.400 mA current. Images were captured with a Canon Powershot A630 digital camera.

The Stereomicroscope (Leica MZ9.5) used in FLBA, was equipped with transmitted light stand, polarizing filters and digital photography and video system (Leica DC300, using Leica IM50 software).

3. Samples and sampling

The weathered Daraki-Chattan quartzite is very friable, so care was taken to obtain grains from a known depth from the surface. The DC-LIR-1 sample (provided by R. Bednarik and G. Kumar) derives from the deeply engraved boulder 'E' in Daraki-Chattan cave (Fig. 1), excavated in 2002 in a depth of 70 cm below ground besides the cave entrance and obviously fallen in an unknown time in the past from an unknown location of the engraved rock surface, with dimensions about 70 cm long, 55 cm wide and 40–45 cm thick. The piece was cut from the boulder under sunlight conditions. The weathered reddish layer has variable depth and the weathering took place while in the sediment.

The cut was initially performed with a rotating wheel (FLBA) and abundance of running water to flatten area to ease further investigations: (a) elemental mapping, thin section, to identify minerals and any weathering product, (b) to produce an appropriate smooth profile for facilitating sampling from top to inner layers (Fig. 2a, b).

Then, in the laboratory under red light conditions, the sample was cut at a section that included part of the groove (Fig. 2c).

In fact, the surface of the rock fragment (about 3 cm × 3 cm × 2 cm) was cleaned with diluted HCl. This surface was then lightly abraded in 1 mm increments up to a depth of 12 mm (12 subsamples) using a medium coarse rasp (#100). The abraded grains of gentle plating of all subsamples were then treated with acetone. No acid treatment was made, thus alphas are included in the dose rate.

Using new rasps, powder was removed per 100 scratch passes in a depth of 12 mm that corresponds to ~4 layers per mm or 0.25 mm/layer.

The grains are coarse, the predominant grain size for area of interest (AOI) the AOI 1 had a mean of 170 ± 90 (1SD) μm and the AOI 2 was below 110 ± 70 μm (AOI: area of interest; defined below in Fig. 3-1). No acid preparation was made.

Two OSL profiles were obtained by depth and removing horizontal layers, from same cobble. In the first profile 45 layers were obtained (Fig. 2b and c gives the exact section in relation to a crack the surficial patina and the ferro-aluminosilicate solution). In the 2nd section 25 layers were obtained (Fig. 2c).

These two sampled sections were taken from different parts of this piece always having patina at the top millimetres from the weathered solution which is spaced out down to depth at least 4 cm with a variable diffusion. The cut pieces were made into thin sections which were divided into five ranges of interest (AOI 1–AOI 5) identifying the removed layers per section on exact scale (Fig. 3-1a, b).

A first mineralogical inspection was made through a stereomicroscope that has produced some interesting images of the rock and loose sand (Fig. 3-2). In fact, inspection of the grains removed for luminescence in the weathered top ~5 mm depth and at 4 cm depth reveals that the weathering solution has impregnated even the deep layers. It is observed that pure quartz grains comprise the major component of this quartzite sandstone and the diffused solution of fallen rock in the sediments has impregnated and coated outer grains in a variable degree while a small proportion of clear grains imply recent deposition from the recurrent solution diffusion.

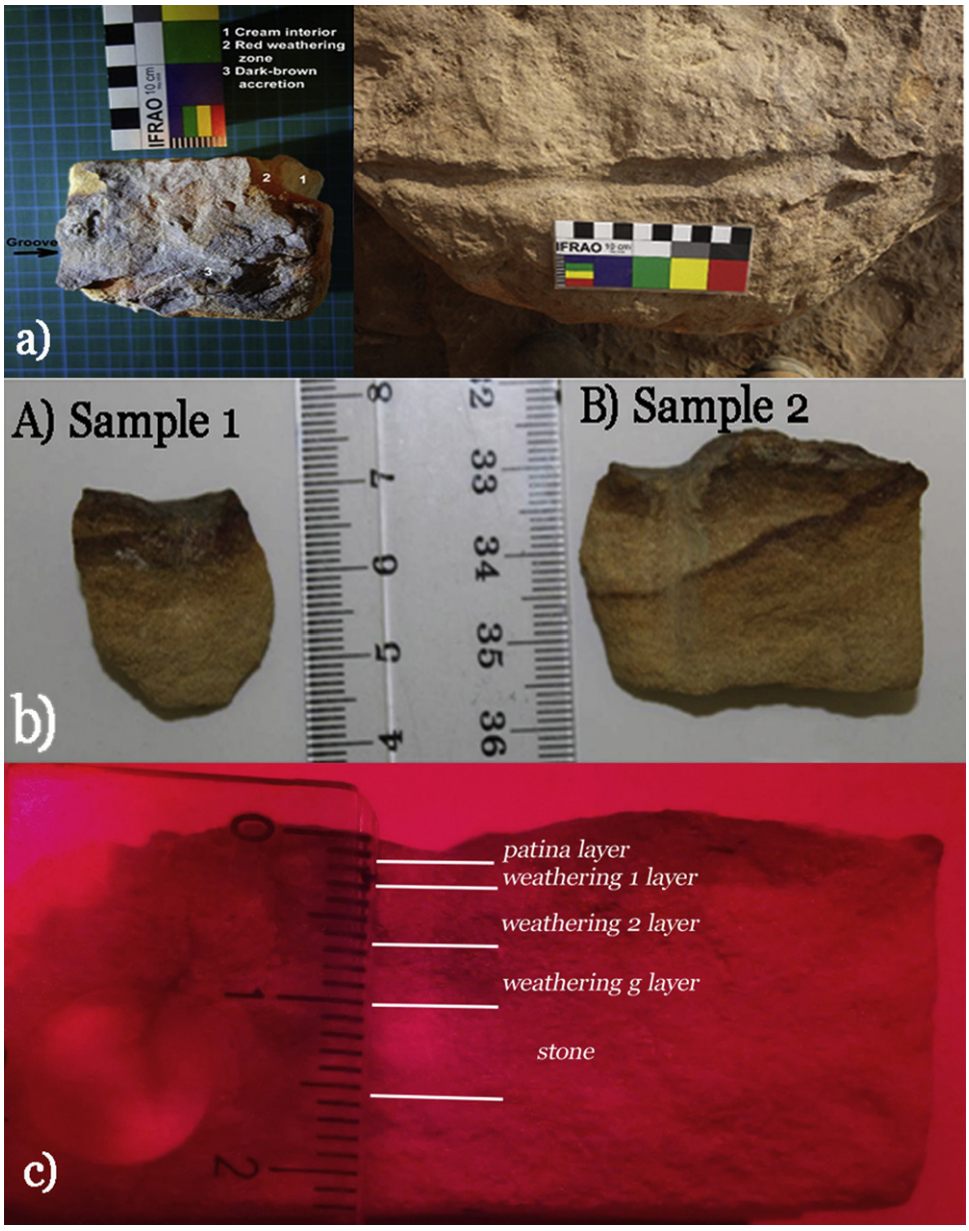

Fig. 2. (a) The cut exfoliated piece (left) removed from boulder E (see Fig. 1) bearing part of the engraved groove (right). (b) The two cut profiles showing upper reddish top patina (A and B). (c) Profile of cut piece in scale (A) that includes a groove, sampled with a rasp from top (patina) down the weathered part and the lower body of the rock.

4. Instrumentation for OSL measurements

4.1. Dating instrumentation

Luminescence measurements were performed using a RISØ TL/OSL reader (model TL/OSL-DA-15), equipped with a high-power blue LED light source, an infrared solid-state laser and a 4.5 Gy/min $^{90}Sr/^{90}Y$ β-ray source. The reader is fitted with a 9635QA PM Tube. All heatings were carried out in a nitrogen atmosphere using a slow heating rate of 2 °C/s, in order to avoid significant temperature lag [19]. OSL measurements were performed using a 7.5 mm Hoya U-340 (λp ~ 340 nm, FWHM 80 nm) filter, transmitting in the 280–380-nm region, with maximum transmittance (57%) at 330 nm. Blue light-emitting diodes (LEDs, 470 ± 30 nm) were used for OSL stimulation; the power level was software controlled and set at 90% of the maximum power of the blue-LED array, delivering at the sample position ~36 mW cm^{-2}. All OSL measurements were performed at the continuous wave configuration (CW-OSL), for 150 s at 110 °C (heating rate also 2 °C/s). For infrared laser stimulation (IRSL), the stimulation wavelength is 875 (±40) nm and the maximum power is ~135 mW/cm^2. The grains were mounted on stainless steel disks using silicon spray. For each sampling layer, two individual measurements were performed.

The a-counter used for the specific measurements is the ELSEC Low Level Alpha-Counter 7286 with an EMI 6097BPM tube, and ZnS(Ag) on mylar film, incorporating an internal 6502 microprocessor and properly calibrated [20].

The alpha counter is used to measure the Uranium-238 and Thorium-232 in samples using the “pairs technique”. The sample was crushed and ground down in a mortar. The powder was sieved in particles finer than 90 μm and dried in a drying oven for 24 h at 60 °C to remove any humidity. Before the measurement, the pulverized samples were placed in specially designed containers and sealed for 4 days to allow build-up of gaseous Radon (Rn-222, half-life $t_{1/2}$ = 3.823 days) [21–23].

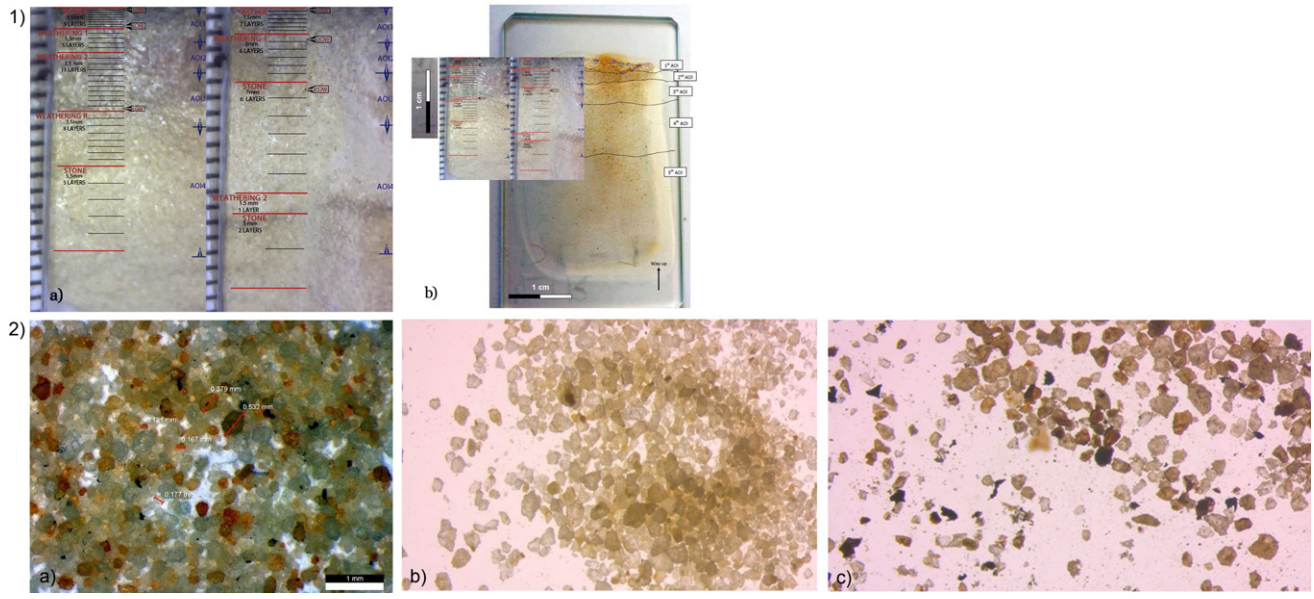

Fig. 3. (1) Thin section of cut smooth face of cobble indicating the various AOI, the layers removed in scale for OSL measurements (a) and the two sampled profiles magnified (b), with depth sampling of 15 mm (38 layers) and 18 mm (22 layers), respectively. (2) (a) loose sand, ×20 with grain size measurements; (b) transmission light of loose quartz from sandstone; (c) transmission light of loose quartz of top weathered layers, under digital stereomicroscope.

4.2. Equivalent dose

The equivalent dose (ED) was estimated by applying the Single Aliquot Regenerative OSL (SAR OSL) protocol [24], after the modifications suggested by Banerjee et al. [25] for polymineralic/mixed quartz-feldspathic samples ('double SAR' method) (Table 1). In brief, each disc was exposed to infrared radiation for 150 s at 50 °C before the laser stimulation (steps 2 and 6). The procedure is similar to the double SAR procedure [25], containing additional SAR steps in order to minimize the need for chemical separation. All signals are integrated over the first second of stimulation out of the 150 s of the entire OSL curve. A background was subsequently subtracted based on the last 5 s (145–150 s) of stimulation. All OSL signals were measured at 110 °C (steps 3 and 7). After the measurement of the natural luminescence signal (NOSL), each aliquot was given a series of increasing regeneration doses in order to obtain a growth curve for each one. Seven different regeneration doses were given, in addition to a zero-dose check for the extent of thermal transfer [22] and a repeat dose point (13 Gy) in order to examine the adequacy of the test dose sensitivity correction procedure (step 0). Regeneration doses were chosen in order to bracket the equivalent dose. The equivalent dose was then estimated by interpolation in the growth curve, as the dose required producing the natural signal.

Table 1
Experimental protocol including all luminescence measurements applied in the framework of the present study. As only OSL was used for the ED estimation, measurements in steps 3 and 7 (in bold and italics) were used for ED estimation (see [21,22]).

Step no.	Explanation
0	Regenerative dose application: 0 (NOSL), 3.3 Gy, 8 Gy, 13 Gy, 27 Gy, 40 Gy, 65 Gy, 100 Gy, 0 (recuperation point) Gy, 13 Gy (recycle point)
1	Preheat at 200 °C (HR = 2 °C/s) for 10 s
2	IRSL at 50 °C, for 150 s
3	***OSL at 110 °C (HR = 2 °C/s), for 150 s***
4	Test dose application: 13 Gy
5	Cut heat at 180 °C (HR = 2 °C/s)
6	IRSL at 50 °C, for 150 s
7	***OSL at 110 °C (HR = 2 °C/s), for 150 s***

The growth curve was fitted for each aliquot by either a linear or a linear-plus-saturation-exponential growth function. Sensitivity changes induced by preheating, irradiation or optical stimulation were monitored and corrected with the aid of a test dose of 13 Gy (step 4), delivered after each regenerative or natural OSL measurement. Before each test dose measurement, a cut-heat at 180 °C was applied (step 5).

Dose recovery results indicated that for all aliquots in both layers, the ratio of the measured to given dose is within ~9% of unity, indicating the suitability of the specified SAR procedure to recover successfully the given β-dose delivered to the samples. This suitability is also strongly supported by the values of both the *recycling ratios*, which lie within the range 0.94–1.05, and the *recuperation*, which is less than 8%. Similar values were also yielded for the recuperation and the recycling values of the natural samples. Individual ED values were accepted based on the following acceptance criteria: recycling ratio between 0.9 and 1.1, recuperation <12%. For the vast majority of the measured aliquots, these criteria were fulfilled.

4.3. Dose rates

4.3.1. In depth dose rate issues

The dose versus depth follows a sigmoid-like trend. Initially is flat (if sun exposed) or gives a flat dose growth. The following upturning curve tends towards a saturation. The few lower doses beyond a peak at the end is probably due to large errors of measurements. An approximate fitting of these curves shows the apparent shape for bleached surface which follows burial in sediment (Fig. 4.1).

For the estimation of age the potassium value from the surrounding sediment is taken from the diffused weathered solution into the cobble measured by SEM, XRF as the average of Table 1 (of main article) that we measured giving K_{av} equal to 1%K_2O = 0.83%K.

K_2O is also estimated from formula relating total beta dose rates (B) in sediments versus K_2O content [26] ($\log B = 0.244–0.024\,K$, $K = K_2O$), equal to 1.5% or $K = 1.25\%$ (on average $K = 1 \pm 0.2\%$).

In fact, there seems an enrichment in radioisotopes for the weathered solution in U and Th which presumably represents the surrounding sediment which in turn seems to have been leached from percolating waters to deeper strata of the excavated

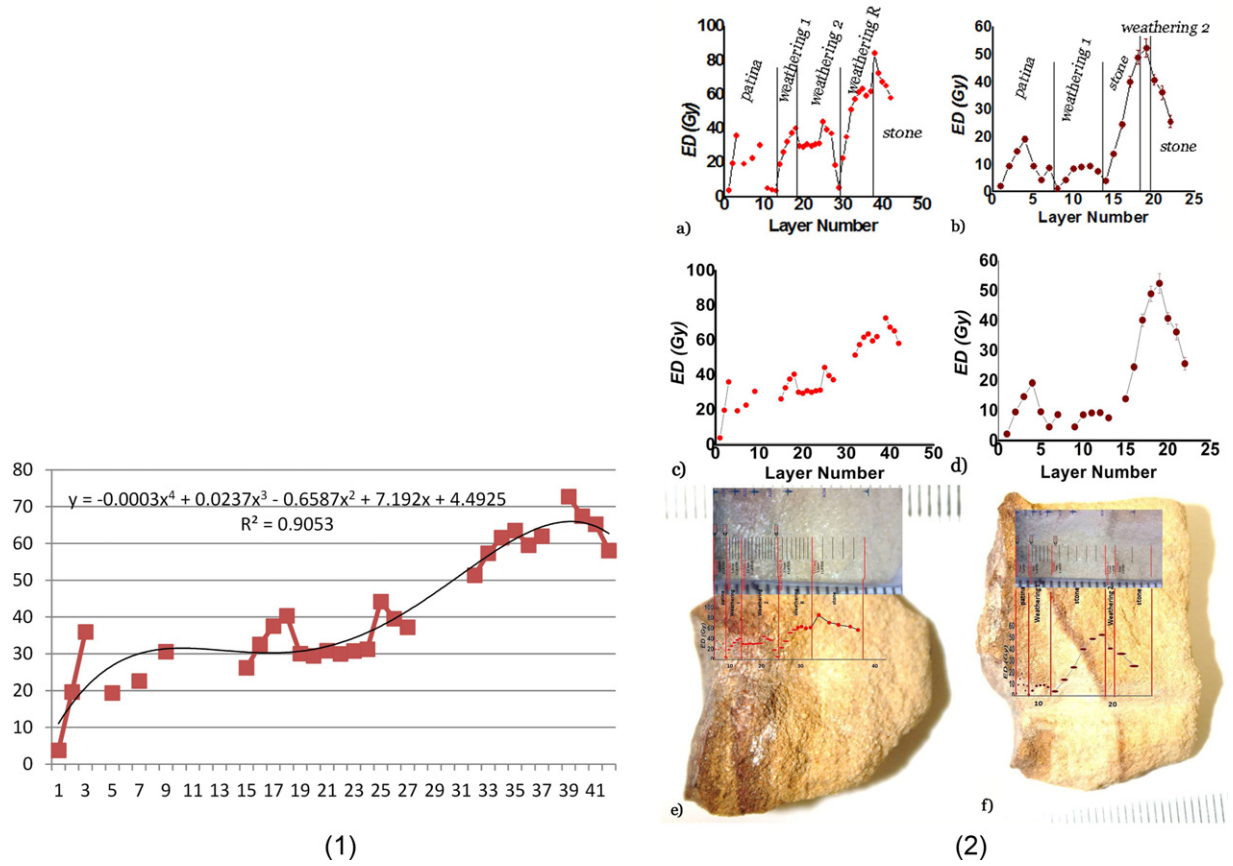

Fig. 4. (1) Indicative trend (zero, flat, exponential-like rise, saturation) by a polynomial fitting. Outliers at lowest and highest level are removed rather due to recent deposition and large coating. (2) The OSL SAR readings per depth for the two profiles (a) and (b) with respective weathering layers; (c, d) same profiles with lower data removed and (e, f) the corresponding setting of dose profiles on the sampled sections. The variation of ED is associated to the three stone zones, patina, weathered and sandstone parts of the two profiles with 15 mm and 18 mm depth sampling respectively.

stratigraphy (Fig. 1 main article, and mineralogical sections below). Hence the average potassium is reasonably a satisfactory value, and on similar rationale the average.

Due to the large dimensions of the boulder where dated piece derives (70 cm long, 55 cm wide and 40–45 cm thick) the environmental gamma ray dose rate contribution Dg to this surficial piece is taken as half of total Dg, the other half comes from the surrounding sediment absorbing water throughout the year because the location of the rock boulder holds water and the water uptake value is estimated as $50 \pm 20\%$, or $w/d = 1.5$ ($D_{g,wet} = D_{g,dry}/[1.14\{w/d - 1\} + 1]$) (coefficients are 1.25 for betas and 1.50 for alphas).

The grains are coarse, the predominant grain size for AOI 1 had a mean of 170 ± 90 (1SD) μm and the AOI 2 and below 110 ± 70 μm. No acid preparation was made.

Attenuation coefficients for alpha and betas per isotope are taken from [27] (their Figs. 2 and 3) as follows: For $\varphi = 170$ μm on average for U and Th it is Da*0.17, and for $\varphi = 110$ μm it is Da*0.20. For the shake of first approximation an average of 0.18 is taken. The respective attenuation for betas per isotope are on average: U: ×0.91, Th: ×0.94, K: ×0.96, Rb: ×0.86). For a 200 μm layer (quartz and coated layer) the average U and Th attenuation for betas is ×0.80.

Regarding luminescent light attenuation through the coated grains and the grain itself light spectra is considered. Spectral attenuation coefficients have been measured for Quartzite (15–20 cm^{-1}) and Orkney sandstone (30–40 cm^{-1}) (from Marc Smillie in 2010; Sanderson pers. comm., March 2018) and applying Lambert's Law of light attenuation $I(x) = Io^{*}\exp(-\mu^{*}x)$, x being the thickness and μ the coefficient, the light attenuation for natural bleaching but also light output from coated grains would explain result of intensity changes of the order obtained in the two dose profiles. In fact, these values would predict about 2–4% attenuation in 10 μm depending on which rock matrix was chosen, with 100 μm layers dropping nearly 40% from the sandstone (~20% out of the system for the quartzite). Thus, a variation between 10–40% in luminescence output of measured quartz and quartz-coated grains is expected. The latter together with the rather lower weathering solution in the 2nd profile would both result in the obtained result of the two dose profiles.

The cosmic ray dose rate dc equals 20 ± 2 mGy/a, it is not included in the NaI reader, and corresponds to an altitude 450 m a.s.l., N 24°32.100′, E 75°43.840′ [28,29]. The cosmic dose rate is conventionally calculated rather than measured, without adjustment for sediment water content. The latitude, altitude and (sediment) depth dependencies of cosmic radiation, and geomagnetic latitude, relevant to luminescence dating, are described by Prescott et al. [28–30]. In the present study, the depth of about 1 m from ground surface of the sample was approximated to few cm. Depth was converted to mass-depth assuming sediment bulk density to be 1.6 g/cm^3, and a fit to the dose rate vs. depth data of [29] was used to calculate the cosmic dose rate at that depth. Uncertainties were calculated as 10% accounting for the variable burial depth occurring over time.

The water uptake values for the sandstone has two effects, (a) the relative humidity entering the few millimetres of stone surface, and (b) the higher humidity carried in by the chemical weathering solution. In the (a) the water uptake varies between 5% and 8% depending from the rock type ([31]; see,

http://www.stonemtg.com.au/choosing%20the%20right%20stone%20for%20the%20job.html). In the (b) within a few millimetres depth the surrounding sediment water uptake remains the same. However, as the seepage of water into the samples increased (increasing moisture content), new pores and fractures are created and the original pores and fractures linked up, resulting in an increase in the number, total area, and diameter of micropores and surface porosity [32].

Moreover, concerning the humidity on rocks, it has been suggested [33] that for igneous rock types the increase of the humidity also brings about an increase in the presence of condensed water by the capillary condensation of water vapour around the crack tips, and thus induces a reduction in the crack growth resistance. It is likely that other rock types that contain few clay minerals (such as the present quartzite sandstone or the Berea sandstone) would be similarly affected [34]. It is therefore possible that the water vapour turns to liquid water by capillary condensation in this zone, and that the crack path close to the crack tip is therefore immersed in liquid water. Since suction therefore occurs between the crack planes by liquid bridging if the crack is immersed in a liquid, compressive stress acts around the crack tip. This suction will decrease with increasing radius of curvature of the condensed liquid. Increase in relative humidity will lead to an increase in the volume of condensed water present. In this case, the radius of curvature of the liquid water will increase as the aperture of the crack increases. The crack tip due to the capillary condensation should be significant.

4.3.2. Radioisotopic content and impact on age

The gamma background radiation readings for the block "E" which was excavated long before the OSL sampling occurred, was estimated from three readings: (a) on the rock surface where the boulder came from (R-1) and from nearby sediment at layer 3 to 4 (DC-4) by NaI (Tl) by portable NaI(Tl) scintillometer calibrated (by R. Roberts Australia), (b) from pairs technique alpha counting of the rock, and (c) from high resolution gamma spectrometry on sediment by A. Singhvi et al. at NRL, Ahmedabad, India.

Once the boulder has fallen into the sediment and eventually being completely covered, the dose rates derive from the weathered quartzite itself whereas the gamma ray component plays a significant part as self-gamma rays dose rate of the large boulder. Then, an additional yet variable radiation is induced by the aluminosilicate oxides diffusing into the rock in the sediment, the cosmic rays and the gamma radiation of the surrounding sediment (Fig. 1b).

In the former case being in situ of the rock the surface luminescence dating version of reduced bleaching as a function of depth and time since concealment is applied [5]. But for the fallen piece that has been sun-exposed prior to being covered by sediment the luminescence of bleached surface is set to zero and grows by time throughout the burial period. Then the accumulated dose defines the time the engraved block "E" became covered by sediment, providing a constrained *terminus post quem* for the rock carving. It works similar to the version used for dating stone masonries in monuments [7,23,35,36].

The alpha and beta radiation from U, Th, and betas from K deposit their energy along their track into the grain size, reduced by an attenuation factor. The water uptake for the site is estimated as 50% throughout the year and the corrected gamma dose rate $D_{g,w}$ from the dry infinite gamma dose rate $D_{g,d}$ is $D_{g,w} = D_{g,d}/(1.14[1.5-1]+1)$.

In addition, the water accompanying aluminosilicate solution transferred through cracks into the interior of the fallen piece exerts an additional added dose and a respective attenuation to the administered radiation to the variable size grains. In fact, the (Fe, Mn)-aluminosilicate carries a variable (U, Th) and potassium content that has been measured by alpha counting pairs technique and SEM/EDS respectively (Table 2). The weathered solution measured as powder from the rock section gave U = 2.73 ± 0.24 ppm and Th = 10.39 ± 0.88 ppm.

As a result, of this effect the ED in quartz gets becomes somewhat complicated; the measured ED comprises of that from the stone itself plus the cosmic, environmental gamma, and from the weathered solution. It is assumed that the intrusion of aluminosilicates into the fallen and presumably cracked piece of quartzite started a very short time interval after the deposition of the block; the measured ED is made from both these sources of radiation (the wet period saturation of the sediments has been observed [3,4]).

In fact, we can see here why diagenetic alteration, recently active, could generate a range of age related artefacts – depending on where the natural and laboratory induced luminescence signals come from. The grains were coated with reddish (Fe, Mn)-aluminosilicate which occurred in situ i.e. is post-depositional. That is, the weathered solution covers grains along their cracked path resulting to a cemented coating of appreciable thickness which obviates luminescence light and their radiation emission to be detected. These effects can explain the ED profiles of Fig. 4. The ED profile with three broad local peaks is in fact very interesting. This is from blue OSL following double SAR where IRSL has been applied to erase light from feldspars. However, attenuation (of daylight during bleaching cycles, or of stimulation radiation) by weathering products is unlikely to be spectrally neutral. The micro-dosimetry of such layered interactions present indeed challenging situations.

Similar effects of Fe staining-coating to quartz has been observed elsewhere [37]. For the estimation of the age the potassium value from the surrounding sediment and that diffused into the boulder is taken as the average of Table 1 that we measured giving K_{av} equal to 1%K_2O. In fact, there seems an enrichment in radioisotopes for the weathered solution in U and Th which presumably represents the surrounding sediment, which in turn seems to have been leached from percolating waters to deeper strata of the excavated stratigraphy (Fig. 2). Hence the average potassium is reasonably a satisfactory value, and on similar rationale the average for U = 2.10 ± 0.30 ppm and Th = 9.60 ± 0.90 ppm. The cracking in the studied rock piece and the diffusion of weathered solution lead to two sampling profiles to check reproducibility of luminescence dose.

5. Age evaluation

The equivalent doses as a function of depth measured by SAR OSL for the two profiles are given in Fig. 4a–f. The depth of the sampling is 15 mm (38 layers) and 18 mm (22 layers) respectively.

The dose at sampling layers corresponds to a particular area of interest (AOI) 1–5, including the low 3–5 Gy EDs (Fig. 4-2a–d the curves and, Fig. 4-2e, f, their setting on the rock piece); the upper top is the reddish patina, followed by weathered zones and clearer sandstone body (see Figs. 4-2a and 3-1b). Fig. 4-2a, b are the original data and Fig. 4-2c, d the remaining ED after intentionally removing some low data.

The first half or so of a millimetre the ED of Fig. 4a, b is zero because the sample was exposed to light during preparation but also ~200 days in daylight after removed from the boulder. The sampling was made on a inner sliced section under red light conditions. The material deeper than 0.5–1 mm is shielded from light. From these preliminary tests it appears that for the two profiles the following observations are made:

1) for the first profile the ~15 layer = ~4 mm and 29th layers the dose is zero (Fig. 4-2a). For the second profile this depth occurs at ~7th and 14th layers (Fig. 4-2b). That is due to the variable sunlight bleaching during the period in situ and from the coating of grains by a ~10–30 μm layer which either obviates or

Table 2
The radioisotope content for U, Th, K, Rb of various instruments used, with sample location and errors from counting uncertainties (for final dose rates, see Table 3).

Sample/method[i]	Sediment[a]			
DC-LIR1	U, ppm	Th, ppm	K[g]	Rb, ppm
NaI, in sediment DC-4 (average 9 readings)[b]	1.78 ± 0.30 (0.125 St. Error Mean)	8.90 ± 0.90 (0.37) ppm	0.43 ± 0.01 ppm	K/Rb = 200, Rb = K/200 = 0.1/200 = ~0.0005–0
HRGS[c]	1.80	9.40	0.42 ± 0.06 ppm	0
From weathered solution in the rock (section 1), Alpha pairs technique[e]	2.73 ± 0.24	10.39 ± 0.88		
Average	2.10 ± 0.30	9.60 ± 0.90		
Sandstone rock[h]				
Alpha pairs technique	0.36± 0.10	2.64 ± 0.33		
NaI against rock surface[d]	1.60 ± 0.08	6.50 ± 0.30	0.10 ppm	
From light weathered solution in the rock (section 2), Alpha pairs technique[e]	0.31 ± 0.12	3.16 ± 0.39		
SEM/EDS, AOI 1			3.30%K_2O	
SEM/EDS and BSE[f] modes, AOI 1, three spots			0.03%K_2O 0.78%K_2O 1.22%K_2O	
SEM/EDS and BSE modes, AOI 2 one spot			0.64%K_2O	
XRF/EDS yellowish fresh section			0.05%K_2O K_2O average = 1.00 ± 0.49	

[a] Gammas from soil DC 4 near DC LIR 1, made by Roberts for the excavators (see footnote g).

[b] The cosmic ray dose rate 0.25–0.30 not included in the NaI (Tl) reader. Cosmic rays dose rate for latitude 24°N and longitude 75°E and altitudes 450 m a.s.l. is estimated as 0.30 mGy/a.

[c] HRGS = high resolution gamma spectrometry on sediment.

[d] Reading with probe against rock wall, next to trench; this includes gammas from skyshine, 2π geometry from rock surface and ground sediment.

[e] Weathered powder from sample profile, with visual reddish colour (Background: 2.44 ± 0.15 counts 108 No. of periods, and for the stone sample: 83.87 ± 0.85 counts (117 No. of periods). In the 2nd section the diluted solution gave U, Th almost similar to sandstone. The counts to content conversion is outlined in the alpha counter calibration paper elsewhere [20].

[f] Scanning Electron Microscope, Backscattered emission spectroscopy.

[g] Colleagues from Ahmedabad NRL India (A. Singhvi et al.) comment that there is a problem with *K* value. It is used to seeing numbers like 1% but since the low (ppm) value is given in numbers by the NaI (Tl) from R Roberts (Australia), they used the same value (Pers comm. 27 February 2016 to Giriraj Kumar from Ashok Singhvi). Here we investigate further this deficiency. At any rate aluminosilicates when subjected to the hydrolysis reaction produce a secondary mineral rather than simply releasing cations, thus leaching potassium e.g.

$$2KAlSi_3O_8 + 2H_2CO_3 + 9H_2O \rightleftharpoons Al_2Si_2O_5(OH)_4 + 4H_4SiO_4 + 2K^+ + 2HCO_3^-$$

[h] The present measured values of U and Th (0.36 ppm and 2.64 ppm respectively) are low, compared to other measurements in literature for sandstones: 4–7 ppm for Th (on average 5.5 ± 2 ppm), and 1–2 ppm for U (on average 1.7 ± 0.7 ppm); while for sand-sized quartz the Th is 3 ppm and U is 1 ppm. Other minerals deposited in hydraulic equilibrium have on average Th = 4 ppm and U = 1 ppm (see, [40]. Sandstone and conglomerate are sedimentary products of weathering, erosion, deposition and cementation, similar to shale. Unlike shale, they seldom have a high content of radioactive minerals when deposited. However, they are much more porous and permeable and often host U and Th minerals deposited by groundwater. This latter case occurs in our boulder exfoliated from the rock art façade.

[i] The various instruments used for gamma ray dose rate were those available to the researchers. Each technique has pros and cons, and the calibration is a most important issue. For U, Th, K the techniques used were the X Ray Florescence = Energy dispersive spectroscopy (XRF-EDS), the Scanning Electron Microscopy – in Energy Dispersive mode for microanalysis (SEM–EDS), the Backscattered Emission spectroscopy (BSE), High Resolution Gamma Spectroscopy using Germanium (HRGS), Sodium Iodine–Thalium activated dopant scintillometer (NaI (Tl)) and the alpha spectrometer using ZnS (Ag) detector and alpha pairs technique.

attenuates luminescence being detected (see discussion below and the mineralogy section). On either sides of this cracked pathed the weathered solution is dispersed as shown in Fig. 2 especially in the section A. In section B OSL profile there appears a tiny cracking path at two points but on either side of those the stone seems to lack the weathered layer. As a result, the dose profile in section B is suppressed with respect to OSL profile section A.

2) an apparently flat dose distribution (within the random scatter) represents the anticipated uniform administration of dose to these layers whose traps were emptied, as long as, the piece was standing in the original position in the rock surface. This is at least a reasonable indication knowing this effect from other studies of rock surfaces, for marble sandstone cobbles. [7,8,18,38]. This flat dose is 20–30 Gy and ~10 Gy respectively for the two profiles. Within the patina and weathered layers some high doses are due to accumulation of higher weathering solution and accompanied radioisotopic content, whereas the induced irradiation is overwhelmingly predominant with respect to luminescence attenuation from any coating around the quartz grains and/or variable natural bleaching due to spectral differences in attenuation (see Section 4.3.1). The variability of isotopic content within an AOI is verified from point chemical analyses by SEM.

The presence of a dose step (parallel lines) in our profile (Fig. 4-2c) means that the first exposure event (*t*1) must have been longer than the second one (*t*2), as it has reset the signal to a deeper depth. In general, such step profiles are only produced if the later exposure event is of shorter or similar length to the previous event(s). Otherwise, the more recent event would completely overwrite the previous profile and thus delete all information on prior events. Therefore, the sequence of events for the rock piece in question here are as follows:

1. Exposure: Our curve follows the data points until a time *t*1, where luminescence is zero for some depth and moves upwards towards saturation.
2. Then rock falls into the sediment and remains there for another time *t*2 and patina and weathering have developed. During *t*2 dose has accumulated from surrounding sediments. The whole curve increases by time for time *t*2 and dose grows uniformly at

a depth ~2.5 mm with different dose rate (curve resembles the pink trend of [15], Fig. 4-2).
3. The ~0.3 mm top ~3–4 layers have been bleached from recent years and preparation exposure, thus the zero to slight increase of dose (Fig. 4-2b).
4. Then at about 25–30 Gy and 15th layer, and ~10 Gy with 16th layer, for the two profiles, the slope changes in a non-linear manner and increases towards deeper layers following the function of luminescence versus depth (Fig. 4-2e, f). The different doses correspond to the variable internal radioactivity of the rock due to weathered solution.

For the estimation of age, the dose rate (DR) from various sources is accounted: the potassium of sediment and the boulder, the U, Th enrichment of weathered solution, as well as, the boulder and sediments are measured applying proper attenuation factors through the grains and due to water uptake, and cosmic ray dose rate too. All these factors are taken into account for in the age calculation and in particular the radioactivity surrounding the grains, weathering diffusion, dose deposition attenuation, water uptake, grain size (see Section 4.3).

The alpha/betas efficiency is taken equal to 0.10 ± 0.02 for coarse-grained quartz [21] and the Rubidium contribution was estimated from the ratio Rb = K/200, where 0.0185 mGy/a = 50 ppm [39].

The dose rate comprises of gamma rays dose rate from the sediment, and the alpha particle and beta particle dose rate from the rock itself plus half of gamma rays dose rate of the rock, finally the cosmic rays dose rate. The half gamma dose rate applies because the surface layers are sandwiched between the rock boulder and the sediment.

The weathered solution added dose has also been calculated using conversion factors for all measured isotopic contents [39].

The first upper layers of two OSL depth profiles which provided the doses of 10 ± 5 Gy and 25 ± 5 Gy are made from variable dose rates but in particular a different coated layer of cemented weathered solution around the quartz grains: 8–10 μm for profile section 1 and a 20–30 μm for profile section 2. For the present purpose the age is taken for the two EDs divided by the different dose rates that the grains are subjected to.

The respective DR is the sandstone and weathered solution diffused into the sandstone for quartz grains having two different thick coated layers. It is 1.70 mGy/a for low coating, hence, the age comes to $14,700 \pm 3000$, and 0.84 mGy/a for high coating that gives an age of $11,900 \pm 3500$ years BP, or an average of 13,300 years BP (Table 3).

The measured U and Th by alpha counting pairs technique [30] on the stone and two weathered part are reported in Table 2. The U, Th contents of the cut section 2 (light weathered medium) are close to those of sandstone.

As a result of seepage of water into the samples through cracks, the ED of grains on either side of the crack is affected, increasing dose rate but decreasing light emission too, while the humidity indeed induces complex micro-dosimetry issues (see Sections 4.3.1 and 4.3.2).

From the above rationale the two ages obtained from the two profiles can be considered close within errors and point to the 13th millennium BP, that coincides with the early post-glacial period or end of Oldest Dryas where cold, begins slowly and ends sharply; although this chronology and following may differ amongst scientists we refer to these within a large error span. It follows from the Antarctic Cold Reversal with warmer Antarctic, and sea levels rise, then 15,000–13,000 BP the Older Dryas cold, interrupts warm period for some centuries and the 14,000–13,000 BP Allerød oscillation warm and moist climatic zones. The drastic change from glacial to interglacial, the rapid retreat of sea ice, caused a sudden end of colder Younger Dryas in ~12th Kyr BP, surely has an impact on the weathering, erosion and exfoliation of rock surfaces. This is mainly caused by the significant temperature change and the resulted thermal differential expansion of rocks by the onset of the Holocene [41,42].

Any OSL dating of rocks should be accompanied by indispensable auxiliary documentation of the mineralogical content and context of the grains within the studied zones, for an accurate as possible total dose (ED) and dose rate evaluation of OSL dating. Primarily in inhomogeneous materials this is a vital task. Below it is outlined the detailed methodological approach including; petrographic data, representative cathodoluminescence images, with SEM/EDS and XRF–EDS analyses, all of which are employed as tools for supplementary/supported data to illustrate the correct methodology devised for the deduction of reliable evaluation of OSL ages, already discussed above.

Indeed, the illustrated mineralogical examination provides data regarding Fe-oxides layers detection of detrital and authigenic quartz implying possible chemical and/or physical changes during growth, the cryptocrystalline nature of clayey and/or cementitious material, the argillaceous material filling of fissures especially in the external surface of the sample, the mineralogical composition, the pure silica content, as well as, the energy of the depositional environment. All these issues relate directly to the status and origin of clay minerals, provide clues of grain size and their context, the internal radioactivity assessment, and help in the evaluation of OSL dating.

6. Petrographic examination

Sample LIR-DL1 was thin sectioned to be examined under a Zeiss AxioScope.A1 polarizing petrographic microscope aiming to characterize it compositionally and texturally. The exterior surface of the analyzed sample is covered by a thin lamination rich in iron oxides and clay minerals. In some places this iron-rich clayey material fills fissures that enter the interior of the rock sample or is deposited in bigger thickness where small depressions occur. The presence of these Fe-oxides impregnates the sample examined towards its interior, diminishing with depth, thus producing a

Table 3
Dose rate (DR), doses (ED) and deduced age for the two sampled sections for OSL.

Section/Lum. data	Da[a] mGy/a	Db[b] mGy/a	Dg[c] mGy/a	DcosmicmGy/a	ED Gy	DR[d] mGy/a	Age	years, BP
Profile 1, high coating	0.032 ± 0.003	0.098 ± 0.015	0.380 ± 0.040	0.20 ± 0.030	10 ± 3	0.84 ± 0.17	$11,900 \pm 3500$	
Profile 2, low coating	0.157 ± 0.016	0.860 ± 0.090	0.376 ± 0.042	0.20 ± 0.03	25 ± 5	1.70 ± 0.30	$14,700 \pm 3000$	
							Mean and St. Er. Mean: $13,300 \pm 2000$ (68.3%)	

[a] Profile 1: the alphas are stopped by the 20–30 μm coated layer around quartz grains with 50% water uptake and due attenuation correction of the grain size plus the coated thickness. Profile 2: the alphas are the sum of weathered solution with little attenuation by a lower thickness located layer of 8–10 μm, both with $50 \pm 20\%$ water uptake.

[b] Profile 1: the sum of the sandstone and heavy weathered solution measured by alpha pairs technique. Profile 2: the sum of lighter weathered solution (0.157 mGy/a) and the quartzite sandstone (0.03 mGy/a).

[c] Both profiles: The sum of gamma ray dose rate from the sediment (0.29 mGy/a) and the rock boulder self gamma dose rate (0.088 mGy/a).

[d] It includes internal radioactivity of quartz 0.1 mGy/a.

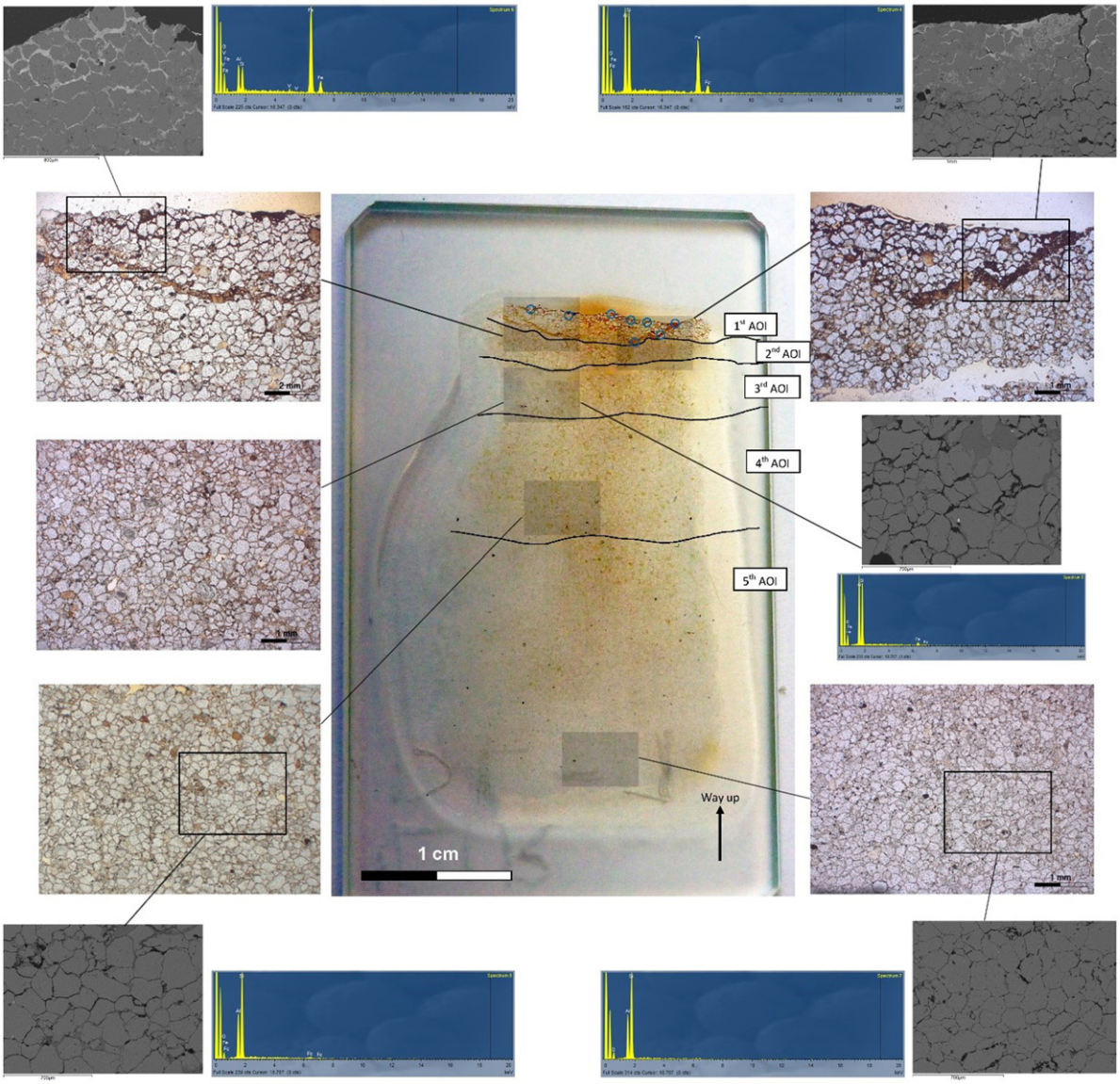

Fig. 5. The various areas of interest (AOI) established in order to control their textural and compositional variability, depicted on the thin section prepared.

variation in the colour hue throughout the sample, from brownish red colours (under plane polarized light; PPL) close to the external surface to lighter yellowish colours towards the interior. In order to characterize in detail the examined sample, five different areas of interest (AOI) were established according to their colour variation (Fig. 5): the 1st area on top with the patina (oxide coating), the 2nd area below with diffusion of aluminosilicate iron-rich solution, the 3rd area as in 2nd but with an apparent crack where solution has been concentrated, the 4th area with slighter diffusion of iron rich solution and the 5th area within the lower layers of the piece. The attribution of 1st layer to a ferromanganese accretion of 1–2 mm thick and variable in thickness that is the coated top layer with the accretion has been analyzed with SEM–EDS.

The petrographic analysis conducted has verified the sedimentary character of the analyzed rock, which due to the dominance of monocrystalline quartz grains can be classified as a typical weathered quartzite (Fig. 6-1a, b).

The reddish-coloured lamination observed in the external surface of the examined rock sample is rich in Fe-oxides and clay minerals which are too fine to be microscopically identified. Small quantities of fine quartz (20–80 μm) and other, sometimes unidentifiable due to their minute size, minerals (e.g. hornblende) are also observed. The thickness of the external lamination is typically around 120 μm but in some areas where small depressions or fissures occur, it reaches an overall thickness of 0.35 mm (Fig. 6-1a–f). The cementing material ranges from rich in Fe-oxide clayey material iron-free aluminium-siliceous from ca. 25 to 15 μm thus highlighting a diminishing degree of impregnation with Fe-oxides towards its depth. The minerals range from 0.10 to 0.25 mm. In terms of mineralogical composition, quartz is the predominant mineral (>95% volume). The analyzed by XRD samples [43] revealed mainly quartz and traces of other minerals. The samples were analyzed by XRD where the scanning area covered the interval 2–70° 2θ with a scanning angle step of 0.015° 2θ and a time step of 0.1 s [42]. The main mineralogical phases revealed were quartz (Qz; SiO_2; ICDD pattern no. 03-06-0466) and traces of birnessite (Br; $Na_{0.55}Mn_2O_4{\cdot}1.5H_2O$; ICDD pattern no. 00-043-1456) and afghanite (Af; $(Na,Ca,K)8(Si,Al)12O_{24}(SO_4,Cl)_3$; ICDD pattern no. 00-046-1264).

In particular, the mineral grains are subangular to sub rounded and only rarely well rounded (very fine to fine sand according to Udden-Wentworth scale), and rarely reaches up to 0.3 mm

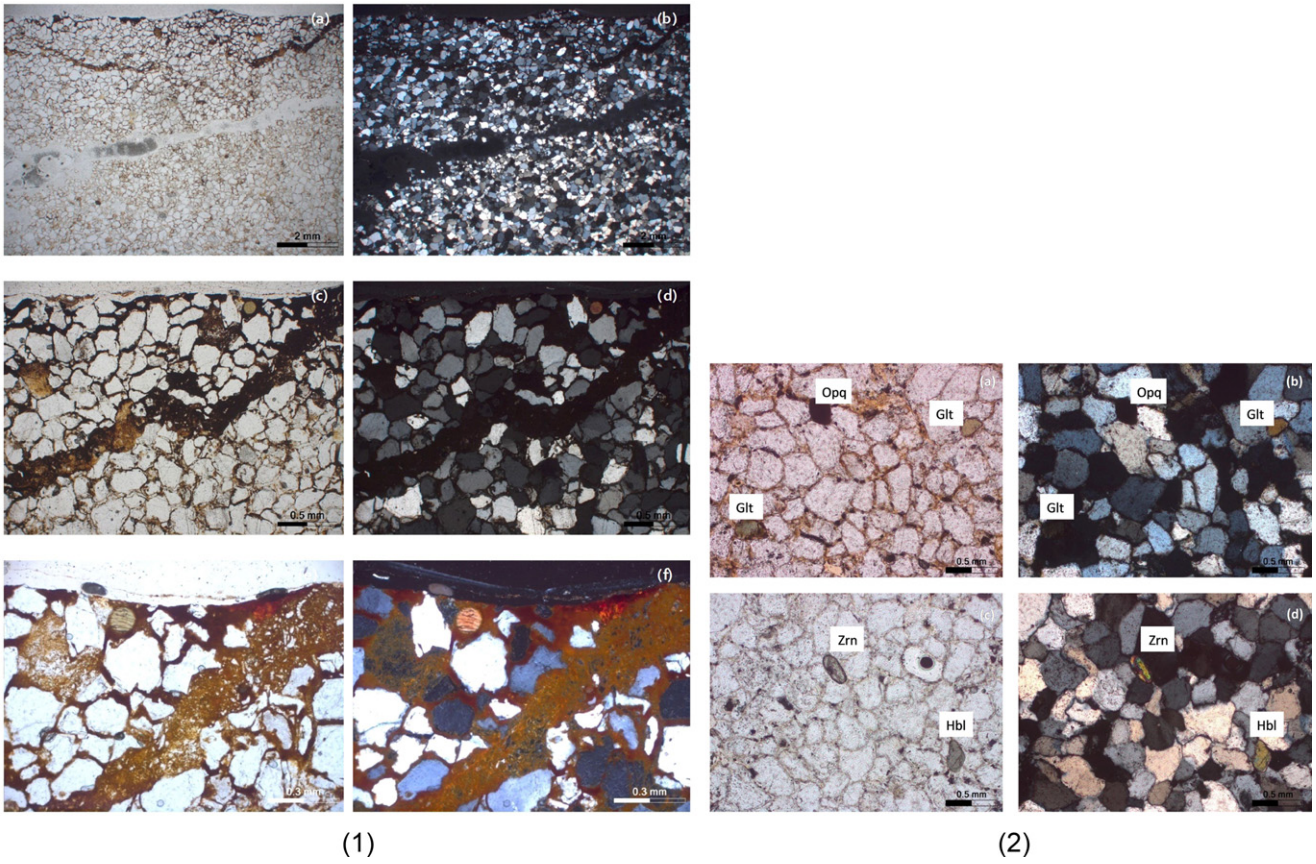

Fig. 6. (1) Representative photomicrographs of the sample examined under the polarizing microscope. Fe oxides are covering mainly the external surface whereas the fissures are filled with clay minerals and Fe oxides. (a) Under PPL; (b) under XP; (c) under PPL; (d) under XP; (e) with the condenser (conical lens) inserted; (f) under XP with the condenser (conical lens) inserted. (2) Representative photomicrographs illustrating the rare presence of some accessory mineral phases. Two grains of olive-green coloured glauconite (Glt) and a dark coloured opaque mineral (Opq) under (a) PPL and (b) XP. A grain of zircon (Zrn) with the characteristic high relief and a green coloured grain of hornblende (Hbl) under (c) PPL and (d) XP.

(medium sand), with the mode being around 0.2 mm (fine sand). Inspite of the overall well sorting of the grains, a slight rhythmic layering of the material due to the grain size variability was recognized in some of the micro-domains of the sample. On the way up, towards the top external surface of the sample, the material ranges from fine-medium sand in the bottom of each layer and reaching fine-very fine sand at the top. This layering is possibly indicating a slight changing in the energy of the depositional environment. In terms of mineralogical composition, quartz is the predominant mineral (>95% volume). Potassium feldspar and plagioclase are rare constituents, with the latter exhibiting in some rare instances a compositional zoning. Argillite fragments were identified in similar quantities as well. As accessory minerals the following were identified: olive coloured glauconite (Fig. 6-2a), opaque minerals (Fig. 6-2b), zircon (Fig. 6-2c), and green hornblende (Fig. 6-2d).

7. Cathodoluminescence

Cathodoluminescence analysis was first performed on the fresh cut surface of the sample prior to thin sectioning as well as after thin sectioning, on both non-polished and polished specimens. A first test with cathodoluminescence to get an idea of the structural status within the piece has shown authigenic quartz (dark cyan-magenta CL colour) overgrowths on detritus quartz (light-bluish CL colour) implying possible chemical and/or physical changes during growth (Fig. 7).

Table 4
Mean chemical analysis of the various areas of interest (AOI) as depicted in Fig. 9, measured through SEM/EDS analysis (LMRR). All analyses are recalculated to a total of 100% on an anhydrous basis.

	AOI 1	AOI 2	AOI 3	AOI 4	AOI 5
SiO_2	88.01	95.37	95.57	97.38	99.12
Al_2O_3	6.18	3.69	4.43	2.62	0.88
FeO	5.81	0.94			

8. SEM/EDS and XRF/EDS analyses

Following the microscopic observation, the thin section was subsequently polished in order to be analyzed by SEM/EDS (LMRR). The backscattered electron micrographs of the various areas of interest are shown in Fig. 8. The mean compositional analysis of the various areas of interest is summarized in Table 4. Additionally, the cementitious matrix of each area of interest was also analyzed and their mean chemical analysis is shown in Table 5. Finally, during the microanalysis of the considered sample, it was possible to identify several mineral phases which were not recognized during the petrographic analysis, namely barite, cobaltoan-tennantite, aluminian-britholite, daqingshanite-(Ce), anatase and manganoan ilmenite, while the presence of zircon was also verified (Table 6).

In AOI 1 a fissure connecting the external area of the sample with its interior is filled with Fe-rich clayey material (Fig. 9) was sequentially analyzed, revealing a noticeable decrease of its iron content (Table 7) towards the internal part of the sample.

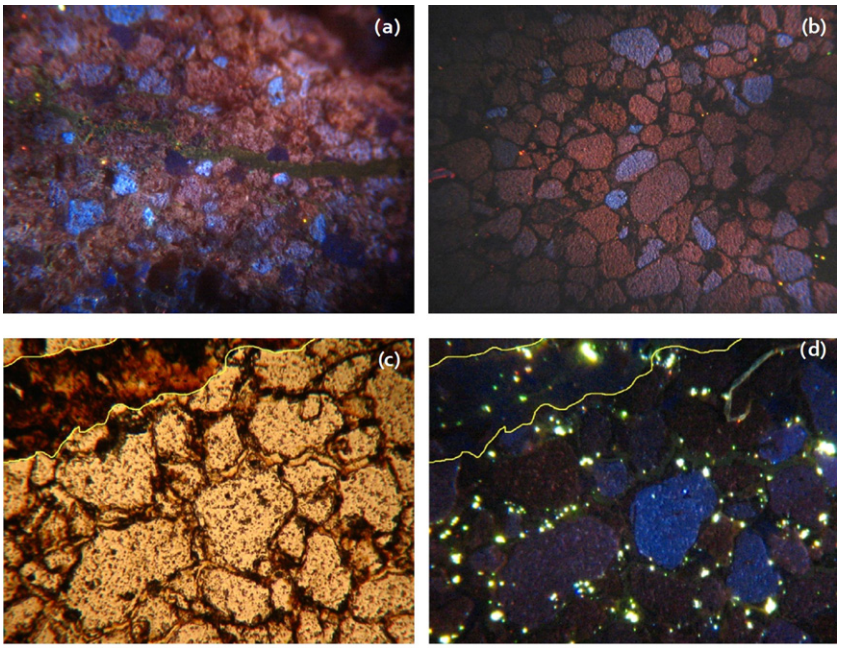

Fig. 7. Representative CL images from the top, rich in Fe-oxides layers (AOI 1 and AOI 2). (a) CL image from the impregnated slab of the sample remained after thin sectioning; (b) CL image from the thin section (non-polished): detrital quartz (light bluish CL colour) is overgrown by later authigenic quartz (dark cyan-magenta CL colour) implying possible chemical and/or physical changes during growth; (c) Photomicrograph under PPL; and (d) its relative CL image illustrating the absence of any cathodoluminescence effects in the joint (depicted with yellow coloured lines) filled with cryptocrystalline Fe-rich clayey material (the greenish yellow coloured areas throughout the CL image are artefacts inherited from the polishing procedure of the thin section). Field of view of (a) and (b) is ca. 2.7 mm and of (c) and (d) ca. 3.7 mm.

Table 5
Chemical variability of the cementitious matrix analyzed in the various areas of interest (AOI), measured through SEM/EDS analysis (LMRR). The analyses given are the mean values of at least five areas of approximately 10 × 10 μm each. Analyses 1a and 1c on AOI 1 are those closer to the external surface of the sample. All analyses are recalculated to a total of 100% on an anhydrous basis. Errors are around 5%.

	AOI 1					AOI 2	AOI 3		AOI 4		AOI 5
	External surface	Reddish coloured		Yellowish green coloured			Fe-poor	Fe-rich	Fe-poor	Fe-rich	
	1s	1a	1b	1c	1d	2	3a	3b	4a	4b	5
Na_2O	3.30										
Al_2O_3	20.0	21.7	30.7	30.10	34.80	40.30	42.9	40.70	42.50	33.40	36.20
SiO_2	65.0	23.7	58.5	36.50	58.50	57.50	57.1	56.10	57.50	65.50	63.60
K_2O	3.30										
TiO_2	1.10			1.30							
FeO	7.60	54.3	10.8	32.60	6.70	2.30		3.20		1.10	

Table 6
Representative analysis of the main accessory minerals identified through SEM/EDS analysis (LRMM) of the various areas of interest (AOI). Errors are around 5%.

	AOI 1	AOI 2			AOI 3		AOI 4	AOI 5		
Analysis	2	2	3	4	2	3	3	1	3	2
	Aluminian-britholite	Barite	Barite	Cobaltoan-tennantite	Daqingshanite-(Ce)	Anatase	Daqingshanite-(Ce)	Zircon	Zircon	Manganoan ilmenite
Al_2O_3	4.6									
SiO_2	6.7							30.9	47.5	
TiO_2						100.0				52.3
P_2O_5	39.3				34.8		31.2			
SO_3		37.1	35.6	39.4			8.9			
MnO										40.5
FeO	11.7									7.2
BaO		62.9	51.7							
CaO					2.5		2.4			
SrO					38.3		45.4			
CoO				4.3						
CuO				52.1						
As_2O_3				4.3						
Y_2O_3	37.7									
ZrO_2								69.1	52.5	
La_2O_3					6.7		3.7			
Ce_2O_3					14.4		6.9			
Nd_2O_3					3.34		1.54			

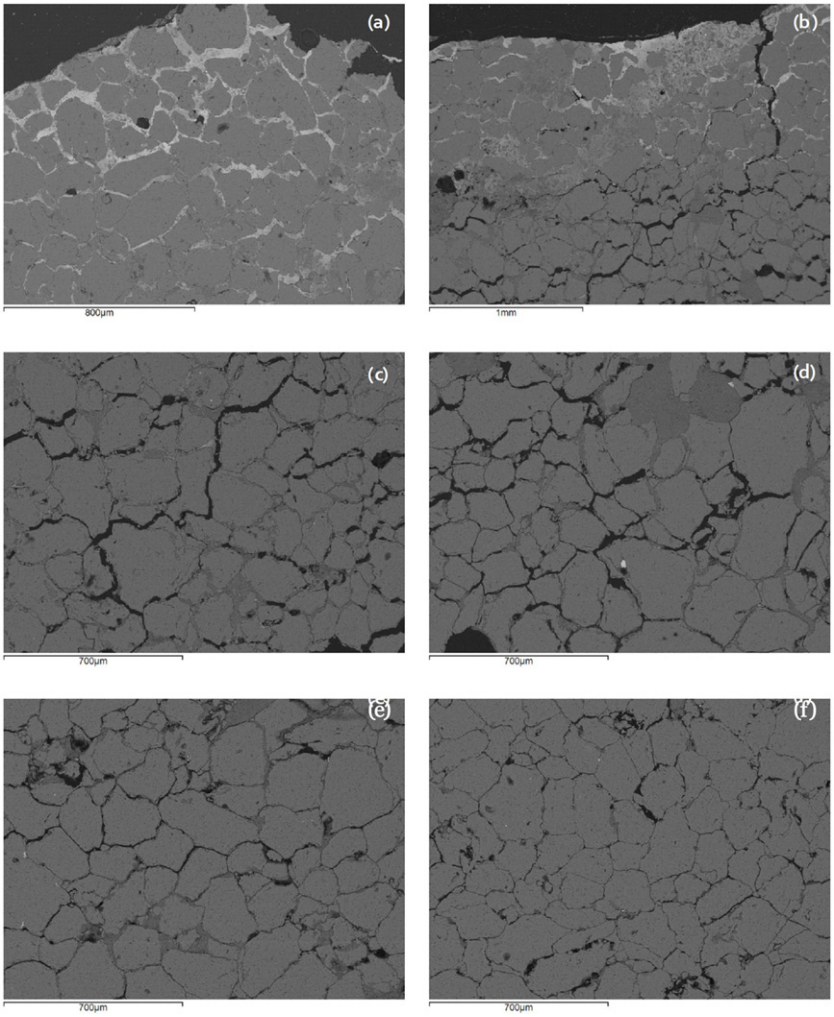

Fig. 8. (a and b) 1st AOI with cementitious material rich in iron oxides and clay minerals; (c) 2nd AOI with cementitious material rich in clay minerals; (d) 3rd AOI with cementitious material rich in clay minerals; (e) 4th AOI with cementitious material rich in clay minerals; (f) 5th AOI with cementitious material rich in silica. All micrographs captured in LMRR.

Table 7
The compositional variability revealed by means of SEM/EDS analysis (LMRR) of the material filling one the main fissures encountered in the AOI 1, connecting the external area with the internal part of the sample. Numbers correspond to the analyses undertaken (see Fig. 9), with 1 being closer to the external surface and 10 towards the interior of the sample (Errors 5%).

Analysis no	1	3	4	5	6	7	8	9	10
Wt%									
Al_2O_3	33.5	33.52	32.18	31.59	30.08	38.81	37.30	40.79	39.93
SiO_2	37.73	38.36	39.82	36.08	38.23	46.95	43.00	53.89	54.14
TiO_2				1.57					
FeO	28.77	28.12	28.00	30.77	31.69	14.24	19.71	5.33	5.93

The chemical composition of the various mineralogical components of the studied sample was further evaluated through spot analysis by means of SEM/EDS (LA) as well as bulk analysis by means of XRF/ED revealing major element oxides supporting findings above (Analytical settings: Analysis area: $10 \times 10\,\mu m$ approximately, collection time: 120 s, accelerating voltage: 20 kV). The chemical oxides of analyzed spots per area of interest (AOI), indicated in the respective image have identified five oxides (Al_2O_3, SiO_2, SO_3, K_2O, CaO, FeO). The study sample is mainly composed of quartz grains from which it inherits its high SiO_2 content. The additional oxides have intruded from the environmental context containing aluminosilicates and iron oxides. Detailed analysis performed on various spots across all areas of interest traced MgO, Al_2O_3, SiO_2, P_2O_3, Cl, CaO, TiO_2, and FeO in individual spots inside AOI 1 (LA).

Further bulk XRF–EDS analysis was undertaken on the cut surface of the sample (yellowish coloured part) before its impregnation for thin sectioning. Several measurements were undertaken both in the reddish coloured outer part of the sample which mainly corresponds to AOI 1 and AOI 2, and in the yellowish coloured part of the sample, which includes mainly AOI 3–AOI 5. The major elements (wt% oxides) revealed were Al_2O_3, SiO_2, TiO_2, FeO, MgO, MnO, CaO, and K_2O taking the average of three runs for each part of the sample. The general trend confirms the results of SEM/EDS analyses.

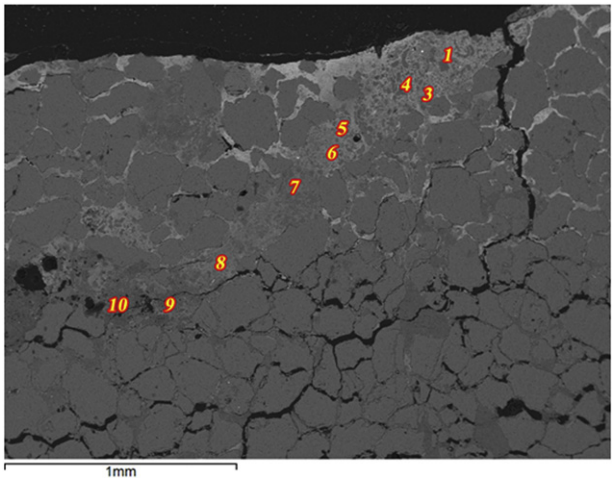

Fig. 9. Chemical analysis by means of SEM/EDS analysis (LMRR) of the iron-rich argillaceous material filling one of the fissures interrupting the external surface of the sample. Each number corresponds to an area of approximately 50 × 50 μm.

9. Discussion

The presented detailed methodological approach regarding minerology that is, petrographic data, representative cathodoluminescence images, with SEM/EDS and XRF-EDS analysis, are shown to have a vital impact in the evaluation of OSL age, evaluated in Age evaluation section. It is shown that those analytical tools are complimentary to each other and support the correct manner to measure dose rates and ED. Hence, for the weathered status of the rock it is deduced a low porosity classifying the sandstone to microporous rocks, where the inter-mineral space is well sealed by aluminosilicates as has been evidenced by our numerous analyses and different techniques employed.

The complete curve of ED versus depth for sampling the rock surface exposed to light in contrast to the rock surface of an exfoliated cobble follows either an exponential, Log-Normal (erf) functions or a double-exponential ones as has been quoted [5,13,36]. Thus, in such case (e.g. rock art, upstanding statue and any other surface continually exposed to solar radiation) the luminescence is reduced, traps are bleached, with depth from surface and with time, and gradually more electron traps below the surface are losing electrons in a non-linear manner (usually saturated exponential or err function). The shape of the bleached curve starts from zero for the monolayer of surface after some hours of sun exposure and increases with depth, but also shifts with deeper layers and the zero surface layers continually are zeroed by depth. For example, for marble within 10 years the zeroed layers are 8 mm and for another marble in 1 year the bleaching occurs in the first 5 mm (Fig. 3, in [13]).

Indeed, several authors have shown that a few minutes [13] to a few hours [8,44] of daylight exposure is enough to bleach the outer 2 mm surface of granitic rocks and for hundreds to thousands of years the bleaching occurs at least to a depth of 7–10 mm for marble and igneous rocks [17,38].

Ideally the calculation of the age that a carved image was made is first, the OSL-depth profile of the known-age sample to be modelled to estimate material-dependent and environmental parameters. These parameters are then used to fit the model to the corresponding data for the samples of unknown exposure history. From these fittings one may approximately calculate the exposure time the buried sample was exposed to light before burial.

Related research using conventional OSL dating may suggest when a rockfall event occurred and so we deduce that the rock art must have been created as a *terminus post quem*. Our results are the first estimates of exposure ages based on luminescence growth-bleaching profile (Fig. 4), for a rockfall age of around 13 Ka.

In the case of the Daraki-Chattan accretion (top patina), this is formed below ground, long after the rock had become covered by sediment, and was precipitated from solution. This accretion consists of aluminosilicates and iron–Mn oxides. The solution diffused into the piece is thought to have occurred since the first wet conditions after exfoliation.

This precipitated accretion has been developed through an unknown time yet during the burial of the boulder. Thus, it was thought to apply OSL of the quartz grains on this but also beneath the accretion, because they would have seen light last time shortly before they became buried.

One could also obtain an exposure age from the luminescence depth profile if the dose data were not scattered due to weathering and if the decay rate at the surface were known. One practical way to obtain an estimate of this is to use a sample of known exposure age for calibration [8,17,18,36,45]. Although we did not have access to such a sample, the present technique can still be used to estimate the relative length of the burial event and approximate the exposure event prior to exfoliation.

Prior to any OSL dating of rock art detailed mineralogical investigation is deemed necessary to understand and properly account for the grain sizes and microdosimetry issues. This is the first time to our knowledge that analysts have had to deal with variable dosimetry and OSL doses due to weathering diffusing through the rock surface. The diffusion of the weathered solution has produced sealed phenomena around quartz grains on a variable thickness which explains the inhomogeneous dose in certain depths of the rock. Further work on non-weathered rock pieces is in progress where the double exponential or err function modelling will fit the doses at the deeper layers (Fig. 4) which correspond to the rock art exposure to the sun since its carving.

Because the OSL data is uniquely interwoven with long term weathering processes it is not possible to relate the present age with the Young Dryas event. Any black mat signature might be found in situ of the resident rock mass. It broadly coincides to the end of the last glaciation, demise of the last ice (Late Glacial and Younger Dryas) and transition to the milder climate of the Holocene.

10. Conclusion

The Daraki-Chattan Indian rock art site has been investigated with OSL and various analytical techniques. The objectives of determination of age of rockfall have been achieved with a detailed supportive methodological approach. The dose and dose rates for OSL age evaluation has been measured following a detailed mineralogical investigation. The rock piece which bears a groove was found buried in sediment. The accumulated luminescence dose since exfoliation defines the time the engraved block “E” has fallen providing a constrained *terminus post quem* for the petroglyph. It works similar to the version used for dating surface stone masonries in monuments. Analytical investigation of the weathered external layer and the intrusion through cracks of aluminosilicate (carrying also P, Fe, Mn, Ca, Ti oxides) and detailed microphotography by SEM explained the dose behaviour in particular depths from top of the rock piece. The analyzed boulder is estimated to have become buried about 13,000 years ago and the rock art is obviously of much higher age.

Acknowledgements

We thank the Director General, Archaeological Survey of India, New Delhi; and the Commissioner, Directorate of Archaeology and

Museums, Government of Madhya Pradesh, Bhopal, for granting us permission for sampling at Daraki-Chattan. We are also grateful to Dr Arakhita Pradhan, Mr Ram Krishna and Dr Manoj Kumar Rathore for helping us to secure the samples (for IL); and to Prof. R.G. Roberts for helping with measuring field radiation in 2004. We thank Dr John Gait, Williams Fellow in Ceramic Petrology, Fitch Laboratory, British School at Athens for help in cutting the rock and stereophotos and most welcome hospitality. IL thanks David Sanderson for useful correspondence on microdosimetry aspects, and Prof. Ashok Singhvi for exchange of ideas on the dose profiles. Dr Andreas Seferlis is thanked for his laborious effort for obtaining the optimum analytical results in SEM and XRF (LEMM). Ioannis Liritzis is thankful for the partial project fund support from Key Research Institute of Yellow River Civilization and Sustainable Development & Collaborative Innovation Center on Yellow River Civilization of Henan Province, Henan University, Kaifeng 475001, China. We also thank the Australia-India Council, Canberra, and the Indian Council of Historical Research, New Delhi, for funding support of the analytical work undertaken.

References

[1] MAA, Mediterranean Archaeology and Archaeometry. Special Issue on Rock Art, vol. 17 (4), 2017, http://www.maajournal.com/Issues2017d.php.
[2] R.G. Bednarik, F. Li, Rock art dating in China: past and future, Artifact 14 (1991) 25–33.
[3] R.G. Bednarik, Palaeolithic art in India, Man Environ. 18 (2) (1993) 33–40.
[4] R.G. Roberts, Preliminary results of the EIP project, Rock Art Res. 22 (2) (2005) 147–197.
[5] I. Liritzis, E. Panou, M. Exarhos, Novel approaches in surface luminescence dating of rock art: a brief review, Mediterr. Archaeol. Archaeom. 17 (4) (2017) 89–102.
[6] I. Liritzis, A.K. Singhvi, J.K. Feathers, G.A. Wagner, A. Kadereit, N. Zacharias, S.-H. Li, Luminescence Dating in Archaeology, Anthropology and Geoarchaeology: An Overview (SpringerBriefs in Earth System Sciences), 2013, http://dx.doi.org/10.1007/978-3-319-00170-8.pdf.
[7] I. Liritzis, A. Vafiadou, N. Zacharias, G. Polymeris, R. Bednarik, Advances in surface luminescence dating: some new data from three selected Mediterranean sites, Mediterr. Archaeol. Archaeom. 13 (3) (2013) 105–115.
[8] R. Sohbati, A.S. Murray, M.S. Chapot, M. Jain, J. Pederson, Optically stimulated luminescence (OSL) as a chronometer for surface exposure dating, J. Geophys. Res. 117 (2012) B09202, http://dx.doi.org/10.1029/2012JB009383.
[9] I. Liritzis, N. Droseros, Light emitting diodes and optically stimulated luminescence dating in archaeology: an overview, Mediterr. Archaeol. Archaeom. 15 (2) (2015) 277–291.
[10] S. Greilich, G.A. Wagner, Light thrown on history – the dating of stone surfaces at the geoglyphs of Palpa using OSL, in: M. Reideland, G.A. Wagner (Eds.), New Technologies for Archaeology, Natural Sciences in Archaeology, Springer-Verlag Berlin, 2009, pp. 271–283 (Chapter 16).
[11] D.J. Huntley, D.I. Godfrey-Smith, M.L.W. Thewalt, Optical dating of sediments, Nature 313 (1985) 105–107.
[12] I. Liritzis, A new dating method by thermoluminescence of carved megalithic stone building, C. R. (Acad. Sci.), Paris t. 319 (serie II) (1994) 603–610.
[13] J. Habermann, T. Schilles, R. Kalchgruber, G.A. Wagner, Steps towards surface dating using luminescence, Radiat. Meas. 32 (5–6) (2000) 847–851, http://dx.doi.org/10.1016/S1350-4487(00)00109-8.
[14] I. Liritzis, Surface dating by luminescence: an overview, Geochronometria 38 (3) (2011) 292–302.
[15] R. Sohbati, Luminescence, Rock Surfaces. Encyclopedia of Scientific Dating Methods, Springer Science+Business Media, Dordrecht, 2013, pp. 1–7, http://dx.doi.org/10.1007/978-94-007-6326-5_83-4.
[16] C. Scarre, Rocks of ages: tempo and time in megalithic monuments, Eur. J. Archaeol. 13 (2) (2010) 175–193.
[17] R. Sohbati, A.S. Murray, N. Porat, M. Jain, U. Avner, Age of a prehistoric "Rodedian" cult site constrained by sediment and rock surface luminescence dating techniques, Quat. Geochronol. 30 (2015) 90–99.
[18] N. Laskaris, I. Liritzis, A new mathematical approximation of sunlight attenuation in rocks for surface luminescence dating, J. Lumin. 131 (2011) 1874–1884.
[19] L. Bøtter-Jensen, E. Bulur, G.A.T. Duller, A.S. Murray, Advances in luminescence instrument systems, Radiat. Meas. 32 (2000) 523–528.
[20] I. Liritzis, A. Vafiadou, Calibration aspects of thick source alpha counter ZnS system, Measurement 45 (2012) 1966–1980.
[21] M.J. Aitken, Thermoluminescence Dating, Academic Press, London, 1985.
[22] M.J. Aitken, An Introduction to Optical Dating: The Dating of Quaternary Sediments by the Use of Photon-stimulated Luminescence, Oxford Science Publications, Oxford, 1998.
[23] I. Liritzis, A. Vafiadou, Surface luminescence dating of some Egyptian monuments, J. Cult. Herit. 16 (2014) 134–150.
[24] M.S. Murray, A.G. Wintle, Luminescence dating of quartz using an improved single-aliquot regenerative-dose protocol, Radiat. Meas. 32 (2000) 57–73.
[25] D. Banerjee, A.S. Murray, L. Bøtter-Jensen, A. Lang, Equivalent dose estimation using a single aliquot of polymineral fine grains, Radiat. Meas. 33 (2001) 73–94.
[26] I. Liritzis, Dating of quaternary sediments by beta thermoluminescence: investigations of a new method, Ann. Soc. Geol. Belg. T. 112 (1) (1989) 197-206.
[27] J.A. Durca, G.E. King, G.A.T. Duller, DRAC: Dose Rate and Age Calculator for trapped charge dating, Quat. Geochronol. 28 (2015) 54–61.
[28] J.R. Prescott, J.T. Hutton, Cosmic ray contributions to dose rates for luminescence and ESR dating: large depths and long-term variations, Radiat. Meas. 23 (1994) 497–500, http://dx.doi.org/10.1016/1350-4487(94)90086-8.
[29] J.R. Prescott, J.T. Hutton, Cosmic ray and gamma ray dosimetry for TL and ESR, Nucl. Tracks Radiat. Meas. 14 (1 & 2) (1988) 223–227.
[30] J.R. Prescott, L.G. Stephan, The contribution of cosmic radiation to the environmental dose for thermolumineseence dating. Latitude, altitude and depth dependences, PACT 6 (1982) 17–25.
[31] B. Behre, K. Littmann, Measurement of humidity in sandstones treated with water repellent agents, in: Hydrophobe V 5th International Conference on Water Repellent Treatment of Building Materials, Aedificatio Publishers, 2008, pp. 75–84.
[32] G.-c. Li, C.-c. Qi, Y.-t. Sun, X.-l. Tang, B.-q. Hou, Experimental Study on the Softening Characteristics of Sandstone and Mudstone in Relation to Moisture Content Shock and Vibration, vol. 2017, 2017, http://dx.doi.org/10.1155/2017/4010376, Article ID 4010376, 14 pp.
[33] Y. Nara, N. Hiroyoshi, T. Yoneda, K. Kaneko, Effect of temperature and relative humidity on subcritical crack growth in igneous rock, Int. J. Rock Mech. Min. Sci. 47 (2010) 640–646.
[34] Y. Nara, K. Morimoto, N. Hiroyoshi, T. Yoneda, K. Kaneko, P.M. Benson, Influence of relative humidity on fracture toughness of rock: implications for subcritical crack growth, Int. J. Solids Struct. 49 (2012) 2471–2481.
[35] I. Liritzis, V. Aravantinos, G.S. Polymeris, N. Zacharias, I. Fappas, G. Agiamarniotis, I.K. Sfampa, A. Vafiadou, G. Kitis, Witnessing prehistoric Delphi by luminescence dating, C. R. Palevol 14 (2015) 219–232.
[36] M.S. Chapot, R. Sohbati, A.S. Murray, J.L. Pederson, T.M. Rittenour, Constraining the age of rock art by dating a rockfall event using sediment and rock-surface luminescence dating techniques, Quat. Geochronol. 13 (2012) 18–25.
[37] A. Singhvi, S.U. Deraniyagala, D. Sengupta, Thermoluminescence dating of Quaternary red-sand debs: a case study of coastal dunes in Sri Lanka, Earth Planet. Sci. Lett. 80 (1996) 139–144.
[38] I. Liritzis, R.B. Galloway, Dating implications from solar bleaching of thermoluminescente of ancient marble, J. Radioanal. Nucl. Chem. 241 (2) (1999) 361–368.
[39] I. Liritzis, K. Stamoulis, Ch. Papachristodoulou, K.G. Ioannides, A re-evaluation of radiation dose rate conversion factors, Mediterr. Archaeol. Archaeom. Spec. 13 (3) (2013) 1–15.
[40] J.J.W. Rogers, K.A. Richardson, Thorium and uranium contents in some sandstones, Geochim. Cosmochim. Acta 28 (1964) 2005–2011.
[41] S. Marshak, Essentials of Geology, W.W. Norton & Company, New York, 2004, pp. 126–127.
[42] C. Harris, L.U. Arenson, H.H. Christiansen, B. Etzelmüller, R. Frauenfelder, S. Gruber, W. Haeberli, C. Hauck, M. Hölzle, O. Humlum, K. Isaksen, A. Kääb, M.A. Kern-Lütschg, M. Lehning, N. Matsuoka, J.B. Murton, J. Noetzli, M. Phillips, N. Ross, M. Seppälä, S.M. Springman, D. VonderMühll, Permafrost and climate in Europe: monitoring and modeling thermal, geomorphological and geotechnical responses, Earth – Sci. Rev. 92 (3–4) (2009) 117–171.
[43] I. Iliopoulos, V. Xanthopoulou, P. Tsolis-Katagas, A petrographic assessment of houseware and storage pithoi in the Early Helladic settlement of Helike, Achaia, Greece, in: D. Katsonopoulou (Ed.), Helike IV, Protohelladika: Helike and Aigialeia, The Southern Greek Mainland, 2011, pp. 127–142.
[44] A. Vafiadou, A.S. Murray, I. Liritzis, Optically Stimulated Luminescence (OSL) dating investigations of rock and underlying soil from three case studies, J. Archaeol. Sci. 34 (2007) 1659–1669.
[45] T. Freiesleben, R. Sohbati, A.S. Murray, M. Jain, S. al Khasawneh, S. Hvidt, B. Jakobsen, Mathematical model quantifies multiple daylight exposure and burial events for rock surfaces using luminescence dating, Radiat. Meas. 81 (2015) 16–22.